ELSEVIER

Contents lists available at ScienceDirect

# Acta Biomaterialia

journal homepage: www.elsevier.com/locate/actbio



# Nitrogen-containing bisphosphonate-loaded micro-arc oxidation coating for biodegradable magnesium alloy pellets inhibits osteosarcoma through targeting of the mevalonate pathway



Mei Li<sup>a,1</sup>, Mengyu Yao<sup>b,1</sup>, Weidan Wang<sup>c,1</sup>, Peng Wan<sup>d,\*</sup>, Xiao Chu<sup>a</sup>, Yufeng Zheng<sup>e</sup>, Ke Yang<sup>f</sup>, Yu Zhang<sup>a,\*</sup>

- <sup>a</sup> Department of Orthopedics, Research Center of Medical Sciences, Guangdong Provincial People's Hospital, Guangdong Academy of Medical Sciences, Guangzhou 510080, China
- <sup>b</sup> Department of Biomedical Engineering, School of Materials Science and Engineering, and National Engineering Research Center for Tissue Restoration and Reconstruction, South China University of Technology, Guangzhou 510006, China
- <sup>c</sup> Department of Orthopaedics, Affiliated Zhongshan Hospital of Dalian University, Dalian 116001, China
- <sup>d</sup> School of Materials Science and Engineering, Dongguan University of Technology, Dongguan 523808, China
- e Department of Materials Science and Engineering, College of Engineering, Peking University, Beijing 100871, China
- f Institute of Metal Research, Chinese Academy of Sciences, Shenyang 110016, China

#### ARTICLE INFO

# Article history: Received 8 July 2020 Revised 29 October 2020 Accepted 12 November 2020 Available online 19 November 2020

Keywords:
Magnesium alloy pellets
Bisphosphonates coating
Osteosarcoma
Multicellular spheroids model
Mevalonate pathway

#### ABSTRACT

Osteosarcoma (OS) remains one of the most threatening primary malignant human tumors of the bone, especially in the first or second decade of life. Unfortunately, the clinical therapeutic efficacy has not substantially improved over the past four decades. Therefore, to achieve efficient tumor eradication, a new approach to prevent tumor recurrence is urgently needed. Here, we develop a new bisphosphonate (BP)-loaded microarc oxidation (MAO) coated magnesium-strontium (Mg-Sr) alloy pellet that can inhibit OS, and we illuminate the cellular and molecular mechanisms of the inhibiting effect. To generate such pellets, nitrogen-containing BP is chemically conjugated with a MAO coating on hollow Mg-Sr alloys. We demonstrate that BP coated Mg pellet has multiple desired features for OS therapy through in vitro and in vivo studies. At the cellular level, BP coated Mg pellets not only induce apoptosis and necrosis, as well as antitumor invasion of OS cells in the two-dimensional (2D) cell culture environment, but also damage the formation of multicellular tumor spheroids by OS cell lines in the three-dimensional (3D) cell culture environment. At the in vivo level, BP coated Mg pellets can destroy tumors and prevent neoplasm recurrence via synergistic Mg degradation and drug release. It is further suggested that the superior inhibitory effect on OS of our pellet is achieved by inhibiting the mevalonate pathway at the molecular level. Hence, these results collectively show that the BP coated Mg pellet is a promising candidate for future applications in repairing defects after tumor removal in OS therapy.

# Statement of significance

Osteosarcoma (OS) is prone to metastases and unfavorable prognosis and the clinical therapeutic efficacy has not substantially improved over the past four decades. It is of high demand in developing new materials that can not only repair the bone defects but also inhibit OS in the lesion location. To solve these problems, we design a hollow Mg-Sr alloy pellet that is modificated with micro-arc oxidation coating and then loaded with Bisphosphonates (BP). Our results of the *in vitro* and *in vivo* biological assays show the inhibition effects and the corresponding signal pathway of BP coated Mg pellets on OS. Our work illustrates the process and mechanism of the tumor therapeutic efficacy for a new biomaterial, which could expand our understanding the ultimate principle of biomaterials-induced tumor therapy.

© 2020 Acta Materialia Inc. Published by Elsevier Ltd. All rights reserved.

<sup>\*</sup> Corresponding authors.

E-mail addresses: wanpeng@dgut.edu.cn (P. Wan), luck\_2001@126.com (Y. Zhang).

<sup>&</sup>lt;sup>1</sup> These authors contributed equally to this work.

#### 1. Introduction

The impact of cancer on the skeleton can be devastating and often results in a major decline in quality of life and reduced survival rates. As the most common primary malignant tumor of the skeleton, osteosarcoma (OS) is characterized by the infiltration of malignant mesenchymal cells and the formation of immature bone stroma [1]. It usually arises from the metaphyses of long extremity bones. Despite its rarity, the negative impact of OS on the youth should not be underestimated due to the peak incidence occurring during childhood and adolescence. Statistics suggest that OS accounts for 15% of all solid extracranial cancers in this age group [2,3]. Advances in surgical techniques, adjuvant therapy and biomedical engineering have led to a major shift away from amputation towards limb-salvage surgery (LSS) for OS [4]. Not surprisingly, randomized controlled trials (RCTs) comparing amputation with LSS showed that LSS results in higher 5-year survival rates and better functional outcomes [5].

For complete tumor removal, the margins of the tumor resection should be at least as wide as Enneking's definition [2]. The resulting tumorous bone defects are usually segmental, and the reconstruction outcome of the patients becomes the key issue during the postoperative rehabilitation process [6]. However, despite no increase in mortality, the risk of local recurrence and mechanical loosening in patients is inevitable. In general, local recurrence is largely due to residual tumor cells at the margins of excision, and a lack of biological or osteogenic activity between the OS prosthesis and bone interface commonly induces periprosthetic osteolysis and fatigue fracture risk under prolonged stress [7,8]. Despite the development of cementless fixation techniques or supplementation with bone grafts leading to relatively ideal results, local recurrence is still as high as 30%, and the failure of an implant in a young survivor varies between 40% and 60% at 10 years [9–11]. Undoubtedly, this dilemma also exists in bone metastases and contributes substantially to morbidity and mortality in patients with advancedstage cancers [12]. Therefore, developing new materials with tumor suppression and bone induction activity applied in primary or metastatic malignant bone tumors is necessarily clinically required. Advancing this research will be expected to increase the long-term stability of limb reconstruction and functional recovery.

In the current study of orthopedic biomaterials, magnesium (Mg) and alloys are considered to be particularly suitable for use as orthopedic fixation without the requirement of surgical removal after healing [13]. This advantage is mainly due to the degradability in the physiological environment, osteogenic activity and close elasticity modulus to the natural bone [14]. Moreover, there have been interesting studies of Mg-based materials for multifunctional applications in orthopedics, such as tumor treatment. As early as 1890, Mg sutures were first used by Nicoladoni to treat hemangiomas. Treatment of hemangiomas via Mg seed and wires had been applied in 27 patients with severely progressive or persistent tumors between 1975 and 1980. A positive result was obtained in approximately 50% of these tumors; however, the mechanisms of tumor treatment were unclear [15–17]. Our research group has previously reported on the inhibition effects on the OS of Mg from the perspective of 2D cell cultures in vitro [18]. We have also illustrated the cellular mechanisms by which zoledronic acid (ZA)loaded Mg-Sr alloys inhibit giant cell tumors, a benign tumor in bone [19]. However, the in vivo results for Mg alloy on highly malignant OS and the corresponding molecular mechanisms are lacking. These findings encourage us to promote and reform the application of Mg in bone tumors.

In addition to surgical operation, drug therapy is the most commonly used adjuvant method to treat malignant bone tumors. It has been reported that bisphosphonates (BPs) have direct antitumor properties and induce OS ossification by bone-specific accumulation [20–22]. In particular, ZA, as a nitrogen-containing bisphosphonate, has shown the most promising results in adjuvant therapy in primary bone tumors and bone metastases. However, there are still some challenges that need to be overcome, especially the systematic side effects in clinical applications, such as renal damage and gastrointestinal side effects [23,24].

To address these issues, we designed hollow Mg pellets based on the as-cast Mg-1.5 wt. % Sr alloys for OS therapy. In our previous study, the Mg-Sr alloy substrate was proven to have matched degradation for bone graft application by tailoring the composition and structure with proper processing and coating [25]. Integrated fracture calluses were formed and bridged the fracture gap without gas bubble accumulation while the substitutes simultaneously degraded. Thus, Mg-Sr alloys are believed to be potential materials for bone filling. In this study, a bilayer-structured coating was fabricated on Mg-Sr alloy pellets, consisting of an outer layer of BP and an inner layer of MAO-derived MgO coating. Therefore, these new pellets integrated the advantage of the osteogenic effect of Mg and the tumor-inhibiting characteristics of BP. The in vitro tumor inhibition of Mg-based pellets was evaluated under twodimensional (2D) and three-dimensional (3D) culture systems, in vivo OS therapy was observed in tumor-bearing mice, and a series of molecular and cellular assays were further used to reveal the responses and mechanisms by which the pellets inhibit OS (Scheme 1).

#### 2. Materials and methods

#### 2.1. Preparation and characterization of Mg alloy pellets

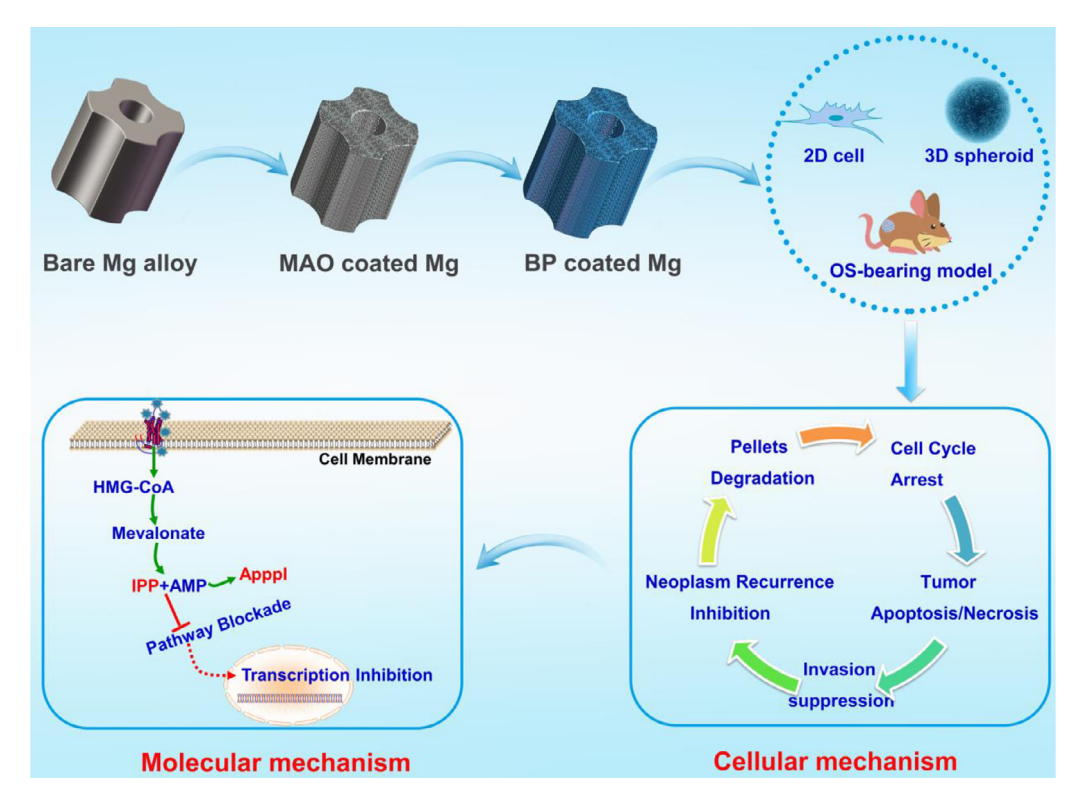
99.9 wt.% Mg and 99.9 wt.% Sr were used to prepare the cast billets of Mg-1.5 wt.% Sr via resistance melting, which was protected by a mixed gas atmosphere (1 vol.% SF<sub>6</sub> and 99 vol.%  $\rm CO_2$ ). Afterwards, they were machined into hollow three-dimensional pellets with reference to calcium sulfate (Osteoset®,  $\rm \Phi 3~mm \times 3~mm$ , Wright Medical Technology), termed "Bare Mg". The details of the preparation procedures can be found in our previous study [26].

Following sanding with SiC paper and cleaning in acetone, MAO treatment was conducted on the Mg-Sr pellets for 5 min using the stainless steel container as the cathode with a frequency of 1000 Hz, a work voltage of 360 V, and a work duty cycle of 40%. The electrolyte was comprised of 8 g L<sup>-1</sup> KF•2H<sub>2</sub>O, 4 g L<sup>-1</sup> (NaPO<sub>3</sub>)<sub>6</sub> and 0.8 g L<sup>-1</sup> Ca (OH)<sub>2</sub>. After preparing the MAO coatings, the Mg-Sr pellets were rinsed thoroughly with DI water and dried by warm air. The resultant Mg-Sr pellets were termed "MAO coated Mg".

A nitrogen-containing BP-loaded MAO coating on the Mg-Sr pellets was prepared due to the strong interactions between BPs and calcium. To achieve this end, MAO coated substrates were immersed into a  $10^{-2}$  M aqueous ZA solution at 37 °C for 24 h through the chemical association of ZA with Ca<sup>2+</sup>. The resultant Mg-Sr pellets were termed "BP coated Mg".

The microstructures of the pellets were observed under a scanning electron microscope (SEM, HITACHI S-4800) equipped with an energy dispersive spectrometer (EDS). *In vitro* degradation of the Mg pellets was described by pH variation and ion release. The samples were immersed in Hank's Balanced Salt Solution (HBSS, Gibco) solution at 37 °C for 14 days with an immersion ratio of 1.25 cm²/mL. The immersion solutions were changed every day, and the initial pH value was set at 7.4. The pH value was monitored every day during immersion. The release of Mg and Sr ions after immersion was estimated using an atomic absorption spectrophotometer (AAS, Hitachi Z2000). The experiments were performed in triplicate.

The hemocompatibility was evaluated by the hemolysis ratio (HR), which was conducted according to the procedure recorded



Scheme 1. Schematic illustration of the applications of BP coated Mg pellets for OS treatment.

in the DIN ISO 10993-4 standard. Normal saline and deionized water were used as the negative control and positive control, respectively. All the reactions were performed in triplicate.

# 2.2. In vitro two-dimensional (2D) tumor inhibitions

The rat OS cell line UMR-106 was purchased from the Type Culture Collection of the Chinese Academy of Sciences and cultured in Dulbecco's modified Eagle's medium (DMEM) supplemented with 10% (v/v) fetal bovine serum (FBS). For Mg alloy extract preparation, the pellets were soaked in DMEM supplemented with 10% FBS at 37 °C for 24 h. The ratio between the area of the pellets and the volume of the medium was 1.25 cm²/mL. The OS cells were seeded into 96-well plates at a density of  $6\times10^4$  cells per cm² and cultured at 37 °C for 24 h, and then the Mg alloy extracts were used to treat the tumor cells for 1, 3 and 5 days. Afterwards, the effects of Bare Mg, MAO coated Mg and BP coated Mg on tumor cell proliferation were determined via CCK-8 assays (DOJINDO).

The cell viability was observed by live/dead staining. Briefly, the tumor cell culture and Mg alloy extract treatments were the same as above. At 1 day, the cell medium was removed, and the adherent cells were subjected to Calcein AM/Ethidium homodimer-1 (EthD-1) staining (Sigma) following the manufacturer's protocol. Afterwards, the stained cells were photographed using a fluorescence microscope (Olympus, BX51).

Cell apoptosis and necrosis were quantified via flow cytometry (FACS). Tumor cell culture was the same as above. After incubating with Mg alloy extracts for 24 h, the cells were collected and stained with Annexin V-Fluorescein isothiocyanate (FITC) and 7-aminoactinomycin D (7-AAD, Millipore) for apoptosis and necrosis detection, respectively. All stained cells were analyzed with a BD FACSCalibur flow cytometer and FlowJo V10.0.7.

The cell cycle distributions were analyzed by FACS. The OS cells in the logarithmic phase  $(2\times10^6)$  were cultured in 6-well plates and incubated with the indicated Mg alloy extracts at 37 °C for 48 h. Afterwards, the cells were collected and fixed overnight with

**Table 1** Primer Sequences for RT-qPCR.

Genes	Forward	Reverse
P27	CCTATTTGGAGAGGTATAGAGTTGT	AGGCATGGCTGAAAAGCAAC
Cyclin D1	TCAAGTGTGACCCGGACTG	CACTACTTGGTGACTCCCGC
Cyclin E	CACAGCTTCGGGTCTGAGTT	GGATGAAAGAGCAGGGGTCC
β-actin	TGAGCTGCGTTTTACACCCT	ATGTTTGCTCCAACCAACTGC

70% cold ethanol at 4 °C. The cells were then centrifuged and washed with ice-cold PBS followed by staining with propidium iodide (PI, 40 mg/mL) and an RNase A solution in the dark for 20 min. Finally, cells with fluorescence were acquired with a BD FACSCalibur flow cytometer, and the distributions of the cell cycle (G0/G1, S, and G2/M phase) were analyzed with FlowJo V10.0.7.

Cell invasion was evaluated by a Transwell system (BD Biosciences) with 8  $\mu$ m pores coated with a Matrigel matrix. A total of  $2\times10^4$  cells were seeded into the upper Matrigel chamber and incubated with Mg alloy extracts (serum-free) for 24 h. A medium with 5% FBS in the lower chamber was simultaneously set as a chemoattractant. Tumor cells invading the opposite side of the membrane were stained with 0.1 % crystal violet (Sigma) and photographed.

SYBR Green Real-time PCR was performed to investigate the relative mRNA expression level of the targeted genes involved in the cell cycle of OS, which was treated with BP coated Mg pellets. Fold changes of the targeted genes were calculated by the  $2^{-\Delta\Delta ct}$  method. The primer sequences of the selected genes are listed in Table 1.

Each of these experiments was performed in triplicate.

# 2.3. In vitro three-dimensional (3D) tumor therapy

OS multicellular tumor spheroids (MCTS) were cultured according to procedures previously described with slight modifications [27]. Briefly, a single-cell suspension of the UMR-106 cell line with

a density of  $10^4$ /well was transferred into U-bottomed ultralow attachment 96-well microtiter plates (ULA plates), which could encourage tumor cell self-assembly into tight cell aggregates. Cells in the ULA-plates were cultured at 37 °C, 5% CO<sub>2</sub> and 95% humidity for 1 day, and then the spent media was exchanged for Mg alloy extracts.

Afterwards, the morphology of the OS MCTS was observed under the microscope and photographed. The cell viability of the MCTS was evaluated by live/dead staining assay. Structures of the spheroid sections were observed via paraffin sectioning and hematoxylin and eosin (H&E) staining. The percentage of cells expressing the nuclear proliferation marker in MCTS was determined based on Ki-67 and p65 immunohistochemical (IHC) staining. Each assay was performed in triplicate.

### 2.4. Mevalonate pathway investigation

The production of mevalonate pathway intermediates, isopentenyl pyrophosphate (IPP) and triphosphoric acid 1-adenosin-5'yl ester 3-(3-methylbut-3-enyl) ester (ApppI), was determined via high-performance liquid chromatography mass spectrometry (HPLC-MS). The accumulation of unprenylated small guanosine triphosphate-binding proteins (G-proteins), RAS-related protein 1A (Rap1A) and RAS homolog family member A (RhoA) was detected by a western blotting assay. Briefly, the OS cells (10<sup>6</sup>/well) were seeded in 6-well plates and pretreated with the indicated Mg pellet extracts at 37 °C for 48 h. Afterwards, the cells were collected and treated with acetonitrile and water containing phosphatase inhibitors. Then, the cells were centrifuged, and the levels of IPP and ApppI in the supernatant were quantified using HPLC. After stimulation with Mg pellet extracts, the cells were washed with PBS and lysed with a radioimmunoprecipitation assay (RIPA) buffer containing proteinase inhibitor cocktail. After centrifugation, the protein concentration in the supernatants was determined using a bicinchonic acid assay (BCA) kit. 40 micrograms of the total protein per sample were fractionated by sodium dodecyl sulfate polyacrylamide gel electrophoresis (SDS-PAGE) and transferred to polyvinylidene fluoride (PVDF) membranes. The membranes were blocked with 5% BSA in a TBST buffer for 1 h at room temperature and then incubated with primary antibodies specific to Rap1A (1:1000), RhoA (1:1000) and  $\beta$ -actin (1:10000) at 4 °C overnight, followed by a horseradish peroxidase (HRP)-conjugated secondary antibody. The proteins were detected and visualized by enhanced chemiluminescence (Bio-Rad Laboratories).

# 2.5. In vivo tumor therapy

Six- to eight-weeks-old male Balb/c nude mice were purchased from the Medical Experimental Animal Center of Guangdong Province. All animal studies were approved by the Institutional Animal Care and Use Committee of Guangdong Provincial People's Hospital. To establish the OS model, a  $1 \times 10^6$  UMR-106 cell suspension was injected into the lower back of the mice. When the tumor size reached approximately 0.5 cm in diameter (approximately 10 days), mice with consistent tumor locations were divided into three groups: the blank control group (tumor resection); the MAO coated Mg pellet group (tumor resection + pellets); and the BP coated Mg pellet group (tumor resection + pellets). Briefly, the Mg alloy pellets were sterilized by cobalt-60 irradiation for use in operation, and eighteen experimental mice were anesthetized by intraperitoneal injection of 3% pentobarbital solution. The back was sterilized with iodine and ethanol and then draped in a sterile manner. A 1 cm incision was made at the right edge of the tumor for tumor excisional surgery. Afterwards, the Mg pellets were used to fill the defects of tumor lesions according to the groupings. To evaluate the characteristics of the Mg pellets in vivo, only one pellet piece was implanted at each excision site. The tumor sizes were carefully recorded every other day for the tumor volume calculation within 28 days. The calculation formula of the volumes (mm³) was  $V=ab^2/2$ , where V (mm³) was the volume of the tumor, a (mm) was the tumor length and b (mm) was the tumor width.

To evaluate the biodistribution of the Mg and Sr ions degraded from the Mg alloy pellets, Balb/c nude mice were sacrificed at 2 and 4 weeks postoperatively. Whole blood and main organs related to organism metabolism, including spleen, kidney, and liver, were collected and digested via aqua regia at 60 °C for 30 min according to the weight to volume ratio. Then, the amounts of Mg ions and Sr ions were measured by ICP-MS and expressed as an ng/kg organ weight according to the reported method [28].

After 28 d, the mice were euthanized, and the tumor tissues and main organs, including heart, liver, spleen, lung, kidney, intestine and brain, were preserved in a 4% paraformaldehyde solution. Following routine tissue dehydration and paraffin embedding, 3.5  $\mu \rm m$  thick sections were cut and subjected to H&E staining and Ki-67 IHC staining to assess tumor inhibition.

The degradation characteristics of different coated Mg pellets implanted in parallel *in vivo* for 2 W and 4 W were observed by micro-CT scanning and 3D reconstruction. To quantitatively describe the corrosion, the weight loss was normally measured after removing the corrosion products in a chromic acid solution (200 g/L  $\rm Cr_2O_3 + 10$  g/L  $\rm AgNO_3$ ) according to the ASTM NACE/ASTM G31-12a standard. Then, the corrosion rate (CR) was calculated according to Eq. (1):

$$CR = (\Delta m \cdot K)/A \cdot t.\rho \tag{1}$$

where  $\Delta m$  is the mass loss, k is a constant equal to  $8.79 \times 10^4$  (mm/y), A is the surface area (cm<sup>2</sup>), and  $\rho$  is the sample density (g/cm<sup>3</sup>).

# 2.6. Statistical analysis

Data were expressed as the mean  $\pm$  standard deviation (SD) from the repeated independent experiments. The significant difference was analyzed using SPSS 13.0. Curves and the histograms were drawn using GraphPad Prism v8.0. The comparisons among groups were evaluated by one-way ANOVA and post hoc multiple comparisons LSD. Statistically, the difference was termed as significant and highly significant at p-values less than 0.05 and 0.01, respectively.

# 3. Results and discussion

# 3.1. Coating characterization

The typical morphology of the MAO coating with micropores on the surface can be observed in Fig. 1A and D. The EDS analysis (Fig. 1B and E) and the corresponding element spectra (Fig. 1C and F) show the apparent peaks of Ca and P, indicating the existence of calcium phosphate deposition. The Mg peak is mainly attributed to MgO formed in the MAO coating. In addition, due to the thick MAO coating, a low content of Sr in the substrate cannot be found in the EDS analysis. After BPs loading, the morphology shows that the depositions covered a large proportion of the surface and that the micropores cannot be seen. The EDS data revealed the existence of Mg, Ca and P peaks in Fig. 1E, and the reduced Ca peak is probably due to dissolution of the Ca-P in the presence of ZA solutions and/or a relatively weak signal.

# 3.2. In vitro degradation and hemocompatibility

The pH curve during immersion for 14 days is shown in Fig. 1G. The pH value of the MAO coated Mg reaches 10 after 1 day and

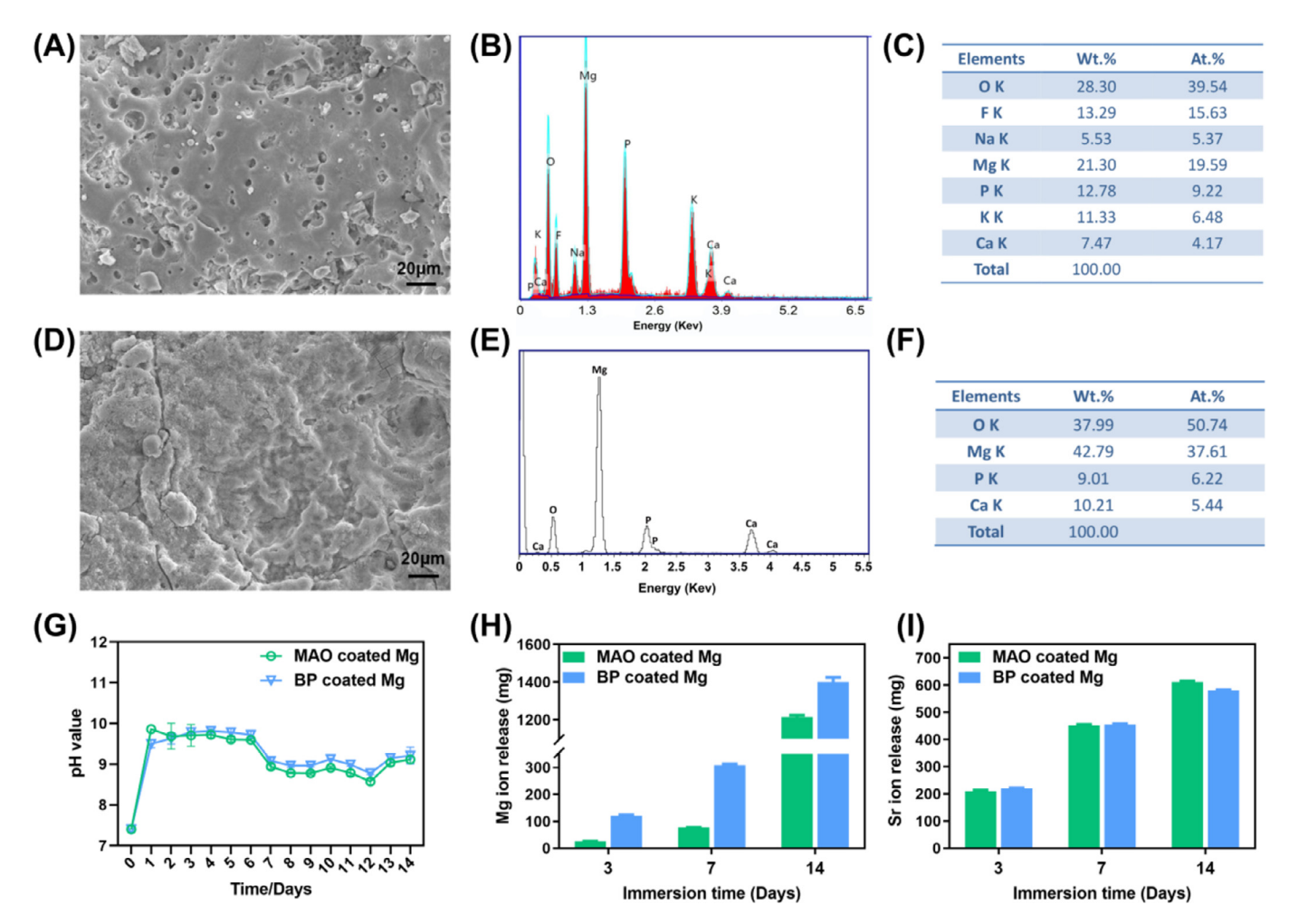


Fig. 1. Surface morphologies and EDS spectra of MAO coated Mg (A, B, C) and BP coated Mg (D, E, F). pH variation (G) and total ion release (H, I) amounts of MAO coated Mg and BP coated Mg after immersion for 3, 7, and 14 days.

then gradually decreases to some extent and finally remains at 9. Likewise, BP coated Mg shows almost the same curve as MAO coated Mg [29]. In addition, the accumulation amounts of the Mg and Sr ions are shown in Fig. 1H and I. The release of Mg ions for MAO coated Mg gradually increases from 25 mg (1 d) to 1215 mg (14 d) with time. Comparatively, the Mg ions released from the BP coated Mg are significantly 4-5 times higher than those of MAO coated Mg. Regarding the Sr ions, there is no apparent discrepancy between the two coatings during the immersion period. The amount of ion release is approximately 200 mg at 3 d and gradually increased to ~600 mg at 14 d. The release of ZA from the BP coated Mg is measured by HPLC, and the results are shown in Fig. S1C. The release of ZA increased continually until day 7, and the highest amount of cumulative release of ZA reached 19  $\mu$ g/mL (65.5  $\mu$ M).

The hemocompatibility of the Mg pellets was investigated by hemolytic activity on red blood cells (RBCs) (Fig. 2A). The positive control group (pure water) turns red because of the hemoglobin released from the RBCs; however, there is negligible hemolysis in all of the Mg pellet groups.

# 3.3. Cytotoxicity and cell viability

The expected sustained drug release encourages us to investigate the therapeutic effect of BP-coated Mg pellets on the OS cells. First, the *in vitro* cytotoxicity of Bare Mg, MAO coated Mg and BP coated Mg was determined on UMR-106 cells by a standard CCK-8 assay. Fig. 2B shows that the survival rate is slightly

lower than 20% for UMR-106 cells treated with BP coated Mg because of BP's toxicity toward OS cells. Then, the cell viability was further investigated by fluorescence live/dead staining. As shown in Fig. 2C, there are negligible dead cells (red fluorescence) in the Bare Mg and MAO coated Mg groups, as most of them are stained green with normal and healthy spindle shapes. More than 80% of the tumor cells in the BP coated Mg group are dead with a round shape and red color, which is consistent with the CCK-8 results. Therefore, these results illustrate an evident tumor inhibition effect of the BP coated Mg. This may be ascribed to the release of nitrogen-containing BPs, which could directly inhibit proliferation and induce necrosis of aggressive OS cells according to previous reports [22,30]. Both the preclinical data and clinical trials have also confirmed that nitrogen-containing BPs could also inhibit tumorinduced angiogenesis and tumor-related osteoclast activity, as well as prevent tumor invasion and metastasis in patients [31].

# 3.4. Cell invasion

Metastasis during OS genesis usually arises from dividing cells detaching from primary tumors and translocating into veins to establish new tumors at distant sites [32,33]. Since OS is highly invasive, most patients eventually develop metastasis, especially pulmonary metastasis, which is still the most prominent reason for OS-caused fatalities. According to statistics, only 10% to 30% of patients could suffer from OS metastasis after surgical procedures combined with chemotherapy. In this way, it is of great importance to prevent OS metastasis with more effective therapeutic methods

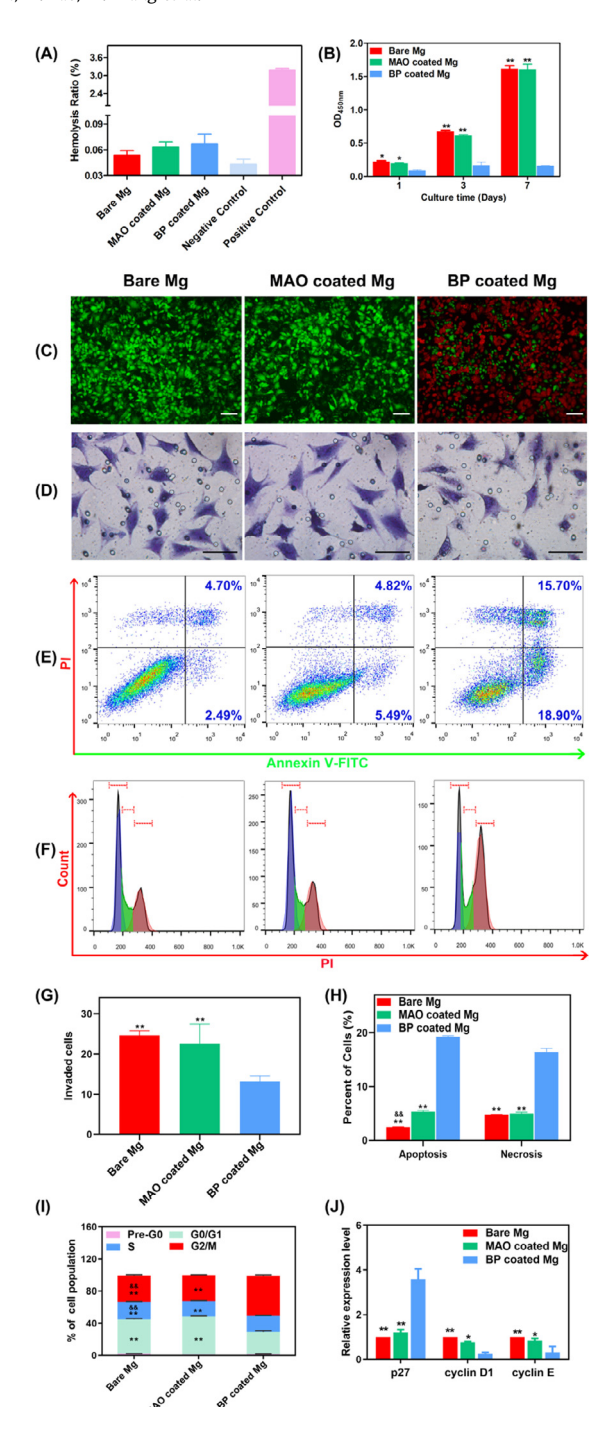


Fig. 2. Hemocompatibility and tumor cell response to biodegradable Mg alloy pellets in an in vitro 2D culture environment. (A) Hemolysis test of the Mg pellets. The hemolysis ratio (HR) indicated that none of our Mg pellets are hemolytic to human red blood cells. (B) Tumor cell proliferation measured by colorimetric CCK-8 assay after 1, 3 and 7 days of incubation with Mg pellet extracts. (C) Representative fluorescent images of live-dead cells detected by Calcien AM and EthD-1 staining after 24 h incubation with Mg pellet extracts. (D) The invasion degree of tumor cells was determined by a transwell system and crystal violet staining after 24 h of incubation with Mg pellet extracts. (E) Tumor cell apoptosis and necrosis verified by Annexin V-FITC/7-AAD double staining and flow cytometry after 24 h of incubation with Mg pellet extracts. The numbers on the upper right quadrant and lower right quadrant represent the apoptosis and necrosis percentages, respectively. (F) Tumor cell cycle distribution analyzed by PI staining and flow cytometry after 24 h incubation with Mg pellet extracts and (G) the corresponding quantification histograms with regards to the percentages of cell population in the pre-G0, G0/G1, S and G2/M phase. (H) Real-time PCR analysis of p27, cyclin D1 and cyclin E mRNA expression in the tumor cells after a 24 h incubation period with Mg pellet extracts. All data are presented as the mean  $\pm$  standard deviation of three independent experiments. \*: p < 0.05 and \*\*: p < 0.01 compared with BP coated Mg pellets. &&: p < 0.01compared with MAO coated Mg pellets. Scale bars represent 50 µm.

and to further improve the prognosis of tumor patients. Based on the invasive process, the Transwell system and Matrigel models are commonly used to evaluate OS invasiveness toward chemoattractants. As shown in Fig. 2D and G, OS cells adhering to the bottom surface of the transwell polycarbonate membrane are stained with a 1% crystal violet, and the microphotographs indicate that cells in the BP coated Mg group invade significantly less (p < 0.01) than those in the other groups, suggesting that the BP coating could inhibit the invasive ability and further metastasis of OS cells.

#### 3.5. Cell apoptosis and cell cycle

To further investigate the effects of programmed cell death induced by the BP-coated Mg pellets, we evaluated the apoptosis and necrosis of OS cells. Programmed cell death is a natural barrier that restricts tumor cells from surviving and diffusing. However, tumor cells usually evolve strategies to evade programmed cell death by generating genetic mutations or epigenetic modifications, and the dysfunction of programmed cell death has been demonstrated to be essential for cancer metastasis [34]. As a typical form of programmed cell death, apoptosis is generally characterized by cell shrinkage, phosphatidylserine (PS) ectropion to the outer leaflet of the plasma membrane, and nuclear fragmentation. Necrosis, however, is characterized by uncontrollable cell damage and spillage of cell contents. Apoptotic cells can only be labeled by fluorescently tagged Annexin V because, as a calcium-binding protein, Annexin V can bind to PS outside of apoptotic cells. However, necrotic cells can be distinguished from apoptotic cells by costaining with fluorescently conjugated Annexin V and PI [35,36]. As shown in Fig. 2E and H, a flow cytometry analysis shows that Bared Mg and MAO coated Mg without drug loading failed to induce apoptosis and necrosis, but cells treated with BP coated Mg extracts could be stained by both Annexin V-FITC and PI, showing that OS cells in the BP coated Mg group are in late apoptosis and necrosis. The difference is significant (p < 0.01).

OS cell cycles treated with Mg pellet extracts were also performed by flow cytometry. In general, the cell cycle is comprised of four continuous phases, G1, S, G2 and M, and culminates with DNA duplication and cell division. Under this definition, tumors are considered to be the consequence of cell cycle disorder, which endows tumor cells with the potential to replicate indefinitely and escape programmed death [37]. This characteristic has been applied in chemotherapy since most anticancer drugs manifest their action via cell cycle phase tailor effects. For example, anthracyclines induce G1, S and G2 phase arrest, while antimetabolites result in S phase arrest [38]. The DNA histograms of our results in Fig. 2F and the relevant statistics in Fig. 2I indicate that the exposure of tumor cells to the BP coated Mg pellet extracts leads to a significant decrease in the Sub G1 fraction and an increase in the  $G_2/M$  fraction compared with other treatments, suggesting that BP coated Mg is cell cycle phase-specific and that G<sub>2</sub>/M cell cycle arrest is involved in the late apoptosis and necrosis induced by the BP released from

To further understand the mechanism of the strengthened tumor cell programmed death and cell cycle regulation by BP coated Mg, we evaluated the mRNA expression level of cell cycle progression-related genes in tumor cells by real-time PCR. The cell cycle phase is known to be tightly regulated by cyclin-cyclin dependent kinase protein (CDK) complexes, such as cyclin D/CDK4 and cyclin E/CDK2 heterodimers [39]. In addition, the cycle process is blocked by CDK inhibitors (CDKIs), including p21/Cip1, p27/Kip1 and p57/Kip2 [40]. As shown in Fig. 2J, in the BP coated Mg group, the expression level of p27 increases, and cyclin D1 and cyclin E decreases significantly (p < 0.05). These molecular expressions lead to cell cycle arrest and are of major importance to prevent tumorigenesis [41]. These data suggest that BP coated Mg could

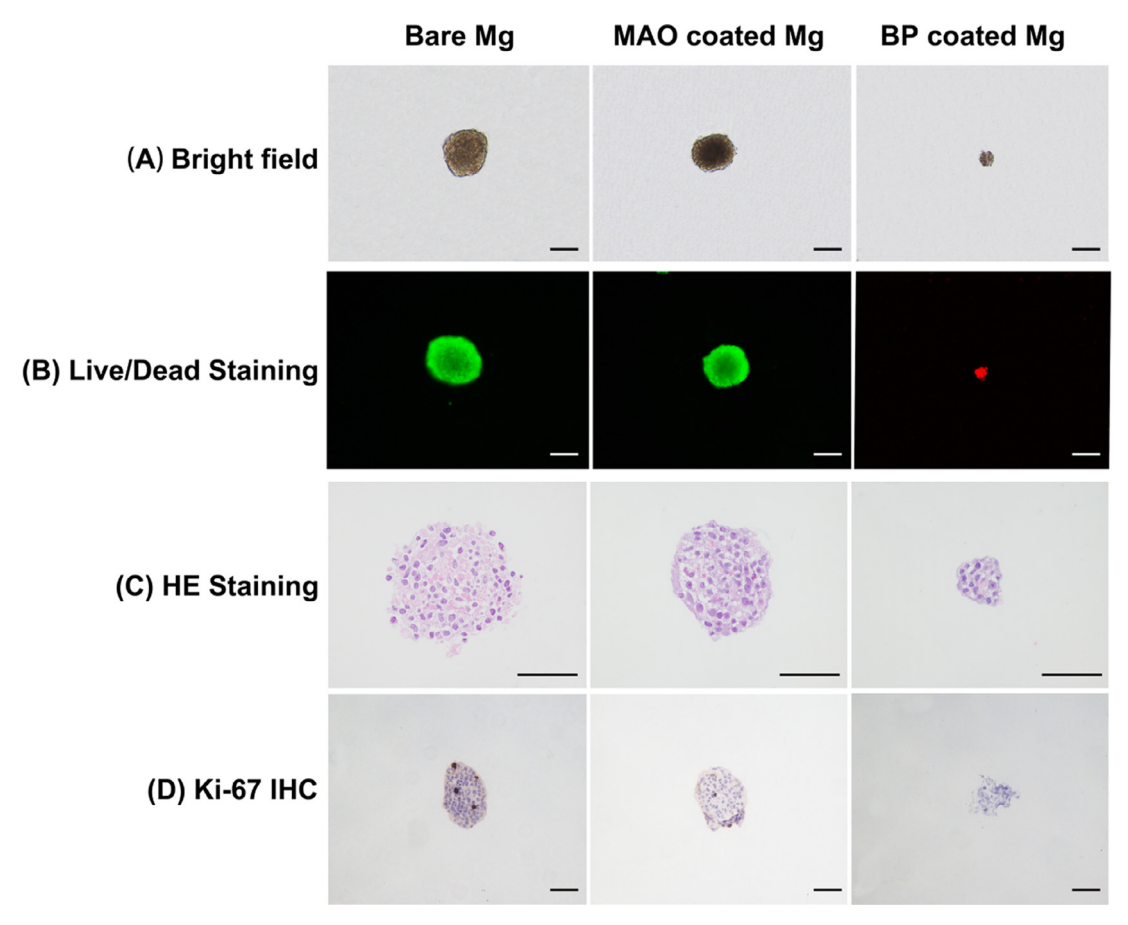


**Fig. 3.** Multicellular tumor spheroid response to biodegradable Mg alloy pellets in an *in vitro* 3D culture environment. (A) Microscopic images of multicellular tumor spheroids formed by the OS cell line UMR-106 treated with different Mg pellet extracts for 3 d. (B) Representative fluorescence imaging of tumor spheroid models exposed to different Mg pellet extracts for 3 d. BP coated Mg induce tumor spheroid necrosis in 3D cell culture. (C) Histochemical characterization and (D) Ki-67 immunohistochemical staining on the OS spheroid interface. Round-shaped structures are cell nuclei, and irregular faint areas represent the ECM. BP coated Mg pellets break the complete histological structure of tumor spheroids and inhibit the expression of nuclear antigens associated with proliferating cells. Scale bar=50 μm.

enhance tumor cell eradication through the regulation of the cell cycle.

# 3.6. Spheroid formation and differential response to Mg pellets

As a kind of solid bone tumor, OS grows in a complex 3D conformation surrounded by various tumor microenvironments, including a low nutrient supply, hypoxia and cell communication with adjacent tumor or nontumor cells [42]. However, tumor cells have usually been cultured in a conventional 2D monolayer environment in previous studies, which resulted in the failed reconstitution of the tumor microenvironment and a deficiency of the original tumor characteristics. With this in mind, there has been a great demand in developing in vitro 3D culture systems, which have the ability to mimic in vivo-like cell behaviors more reliably, including the 3D architecture and cellular connections. In our present study, OS cells were cultured as MCTS in vitro to recapitulate solid tumors from the perspectives of cell-cell or cell-matrix interactions, the gradient distribution of oxygen and drug penetration limitations. This is the first time that the MCTS model represents the avascular regions in OS tissues to be used in evaluating the effect of Mg alloys on tumor inhibition. Fig. 3A shows representative optical photographs of MCTS treated with different Mg pellet extracts. Apparently, the OS cells spontaneously form stable MCTS with a round and compact shape and a mean size of 120  $\mu$ m. Fig. 3B shows that there are no inhibitory effects on the growth or integrity of MCTS treated with Mg pellet extract and MAO coated Mg pellet extract at 3 d. In contrast, the stimulation of BP coated Mg extract results in a significant inhibition of MCTS growth at 3 days, which is characterized by a decreased size of the spheroids and less compactness of the outer layers. To investigate the effect of Mg pellets on MCTS viability, live/dead staining (Calcien AM/EthD-1) was performed on the 3D spheroids. Fluorescent photographs (Fig. 3B) show that all survived cells are labeled with green fluorescence in Bare Mg and MAO coated Mg groups. However, all died cells are labeled with red fluorescence in the BP coated Mg group. These viabilities are almost consistent with the 2D culture results in vitro, and the inhibition effect is much more significant in the 3D environment. To observe the interior histological characterization of MCTS, spheroids were embedded in paraffin and stained with H&E at day 3. As shown in Fig. 3C, MCTS treated with Bare Mg extract and MAO coated Mg extract present a dense and compact cellular distribution, whereas spheroids show irregular and loose connections in the BP coated Mg group. Furthermore, to assess the validity of these results, the proliferative cell marker Ki-67 was immunostained for the 3D spheroids. Fig. 3D shows that the majority of Ki-67-positive cells are mainly located on Bare Mg and MAO coated Mg group but are very rare in the BP coated Mg group. In summary, this OS spheroid system could mimic the architecture of the tumor properties, especially the interaction of the cell-cell and cell-matrix. We demonstrated the inhibitory effect of BP coated Mg on OS in a 3D environment and that the performance of OS cells is slightly different from the monolayer experiments, especially the cellular activity.

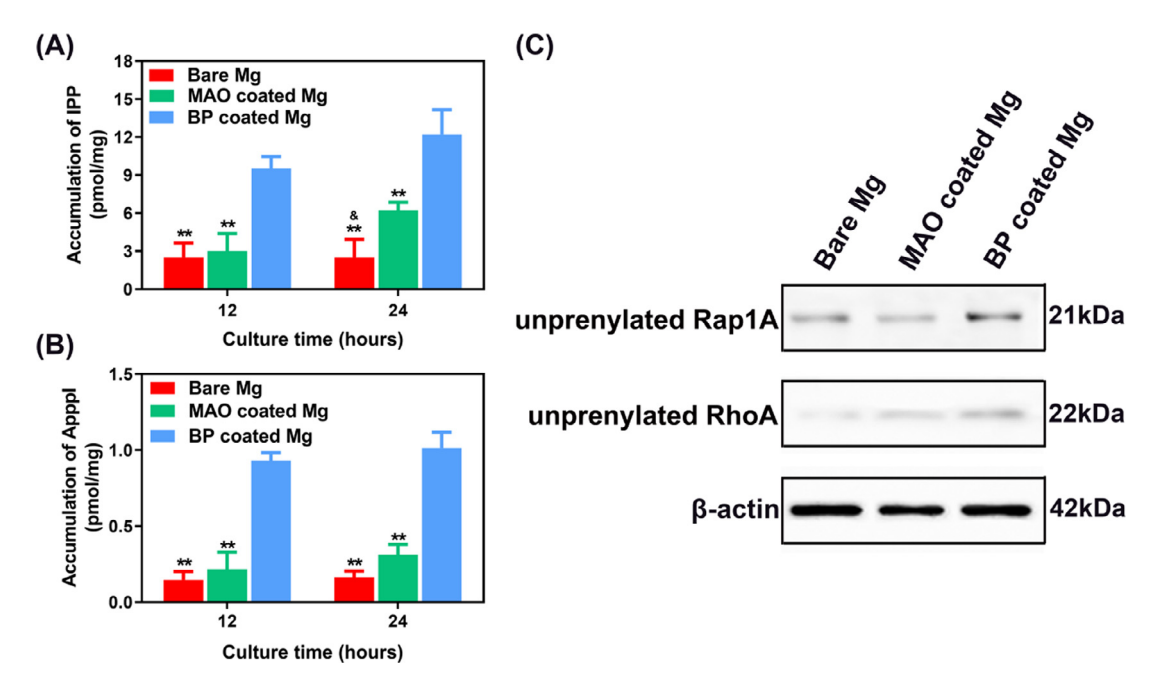


**Fig. 4.** Influence of biodegradable Mg alloy pellets on the mevalonate pathway of OS cells. (A) The intracellular accumulation amount of the metabolites IPP and (B) Apppl in tumor cells incubated with different Mg pellet extracts at 12 and 24 h measured by HPLC-MS; (B) The accumulation of unprenylated Rap1A and unprenylated RhoA in tumor cells incubated with different Mg pellet extracts at 24 h performed by western blot analyses. All data are presented as the mean  $\pm$  standard deviation of three independent experiments. \*\*: p < 0.01 compared with BP coated Mg pellets and <sup>&</sup>: p < 0.05 compared with MAO-coated Mg pellets.

#### 3.7. Regulation of the mevalonate pathway

The mevalonate (MVA) pathway is a core metabolic pathway that provides essential molecules for important cellular processes, such as cholesterol biosynthesis and G-protein prenylation. That is, the MVA pathway is fundamental for cell metabolism, growth and survival [43]. Accordingly, this pathway has been involved in multiple aspects of tumorigenesis [44]. As a result, targeting the MVA pathway emerges as a promising approach for tumor therapy [45]. Recent studies have reported that the multiple effects of BPs on tumor cells are primarily through interference with the MVA pathway. Specifically, nitrogen-containing BPs is known to inhibit farnesyl pyrophosphate synthase (FPPs) in a dose-dependent manner, which leads to an accumulation of IPP [46]. This intermediate can be further metabolized into a pro-apoptotic ATP analog, ApppI [47]. IPP/ApppI production further decreases the geranylgeranylation and farensylation of small G-proteins, such as Rap, Ras and RhoA, and eventually leads to anti-neoplastic efficacy, including apoptosis, necrosis, cell cycle arrest and anti-invasion [48,49]. To confirm whether BP coated Mg pellets act through the MVA pathway in OS, we measured the accumulation of extracellular IPP and Apppl via HPLC-MS, as well as the expression level of unprenylated proteins Rap1A and RhoA by western blotting in UMR-106 cells. Fig. 4A and B shows that BP-coated Mg induces significant accumulations of IPP and ApppI after incubation for 12 h and 24 h in comparison with Bare Mg and MAO-coated Mg (p < 0.01). However, there is a slight elevation of these two metabolites in the MAO coated Mg group at 24 h compared to 12 h and there is almost no increase in Bare Mg group. Along with this IPP/APPPI intermediate production, upregulation of unprenylated Rap1A and RhoA is obviously observed in the BP coated Mg group compared to the others (Fig. 4C). Insufficient prenylation of the G-proteins results in impaired cell function and induces the death of tumor cells [50]. Therefore, regulation of the MVA pathway is the major mechanism induced by BP coated Mg that ultimately triggers OS inhibition.

#### 3.8. In vivo tumor therapy

As a typical malignant bone tumor, the 5-year survival of OS is approximately 70%. However, it rapidly declines to 20 to 30% in patients with local recurrence and metastases, which further increases the amputation rate [1]. Therefore, the elevated significance of the effective treatment and repair of OS should be emphasized. Surgery resection generally has difficulty thoroughly eliminating tumor cells in LSS for OS patients. Residual OS cells always survive and further invade the surrounding healthy bone tissues [51]. This puts forward a new request and new opportunity to design and develop new biomaterials for suppressing residual OS cells while simultaneously enhancing the repair of neoplastic bone defects postoperatively by using a safe and effective protocol. To our knowledge, there are very few studies on this type of biomaterial. In our present study, the tumor inhibition effect of BP coated Mg was also investigated in vivo, which lays the foundation for future antitumor applications. The visual images of residual tumor tissues in different Mg pellet groups at 28 d post implantation, and more details of the tumor volume and body weight during the therapy period are shown in Fig. 5. Tumors in Bare Mg and MAO coated Mg groups grow rapidly, and the tumor sizes are large due to the highly malignant properties of OS. In contrast, there are only small scars on the surgical site of the mice in the BP coated Mg group, and the tumor volume is significantly reduced compared to other groups, indicating a noticeable tumor inhibition effect. Furthermore, Fig. 5D shows that the body weight of the mice during the therapy always lies between 18 and 24 g, and the difference is not significant; however, mice in the unsatisfied treatment group become weaker as the tumor size increases.

H&E staining of tumor foci sections (Fig. 6A) indicates that tumor cells show typical pathological characteristics of OS, and a clear vascular structure (indicated by yellow colors) can be seen in the Bare Mg and MAO coated Mg group, demonstrating the negligible therapeutic effects and recurrence of tumors, which are consistent with the tumor volume changes (Fig. 5C). For the BP coated Mg group, severe damage to the tumor tissues and irreversible

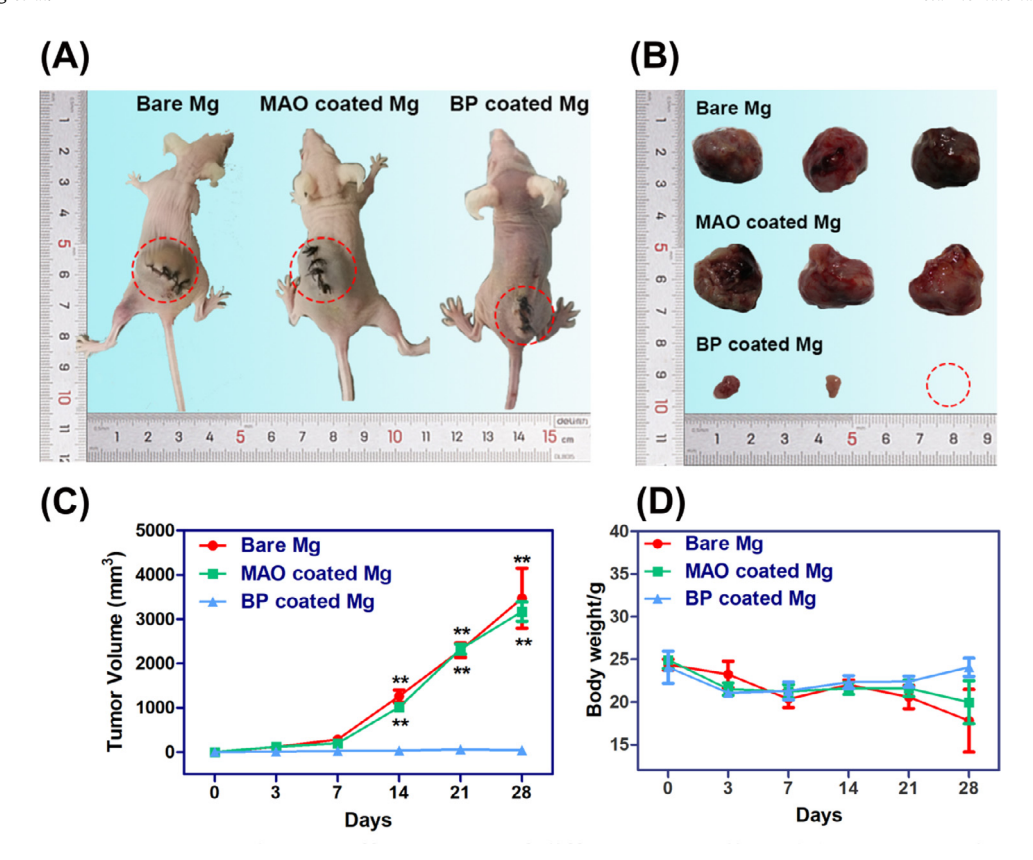


**Fig. 5.** *In vivo* therapy effect on OS of different Mg pellets. (A) Representative photos of tumor-bearing nude mice in different groups 28 days after Mg treatment. In the BP coated Mg pellet group, there is only a small scar on the back of the mouse, and the tumors are totally suppressed. (B) Tumor tissues collected from mice treated with different Mg pellets at day 28. (C) Tumor volume growth curves of different treatment groups within a 28-day period. The tumor volume of BP coated Mg pellet group is significantly lower than those of the other groups. All data are presented as the mean  $\pm$  standard deviation of three independent experiments. \*: p < 0.05 and \*\*: p < 0.01 compared with BP coated Mg pellets. (D) Dynamic change curve of the mouse body weight in different treatment groups during a period of 28 d.

necrosis are identified around the pellets, including atrophic tumor structures, disappearance of cell nuclei and ambiguous intercellular gaps.

Furthermore, to measure tumor cell proliferation in vivo, proliferating cell nuclear antigen Ki-67 and transcription factor p65 (RelA) of the NF- $\kappa$ B family are immunohistochemically labeled. As a nuclear DNA binding protein, Ki-67 is a widely used marker for tumor proliferation and grading. A high Ki-67 index generally shows poor prognosis in clinical conditions [52]. On the other hand, as a transcription factor, p65 could regulate the transcription of genes and plays an important role in tumorigenesis, tumor development, infiltration and metastasis by binding to the gene promoter regions [53]. Fig. 6B and C show that Ki-67 and p65 are highly expressed around the pellets in Bare Mg and MAO coated Mg groups (indicated by brown or dark brown colors), suggesting the rapid growth of OS cells. For the BP coated Mg group, the expression of Ki-67 and p65 is negative (indicated by central blue colors), demonstrating a significant inhibitory effect on the cell proliferation of OS [54]. The in vivo biocompatibility of Mg pellets is further investigated by H&E staining of the main organs in mice, including the heart, liver, spleen, lung, kidney, intestine and brain. As shown in Fig. 7, there is no inflammatory response or tissue damage in any group. Therefore, all these results suggest that BP coated Mg has advantages in OS therapy and prevention of postoperative recurrence over traditional therapy.

The highly efficient therapeutic effect for inhibiting OS *in vivo* is mainly attributed to the BPs released from the Mg pellets. Previous studies have indicated that BPs exhibit pH-dependent cellular toxicity [55]. For the biodegradable drug carrier, Mg is beneficial for the antitumor effects of BPs because of the alkaline environment

produced by degradation. In addition, the in vivo satisfactory osseointegration effect of the Mg-Sr alloy substrate has been proven in our previous studies [25]. In our present study, BP coated Mg also promotes osteogenic differentiation and extracellular matrix mineralization, as well as the expression of osteogenesis-related genes in bone marrow mesenchymal stem cells (BMSCs), as shown in Fig. S3. In addition, osteoclast- mediated bone resorption and a decreased loss of bone mass could also be inhibited by BP administration [29]. Additionally, the use of BP coated Mg alloy pellets could reduce the BP dose compared to conventional therapy, such as intravenous injection, and effectively avoid the side effects of systematic use [24]. It is interesting that presently, BP injection provides a therapeutic alternative for patients with metastatic bone cancer in the clinic. That is, BP is effective for bone metastasis. Therefore, our BP coated Mg has the potential to promote neoplastic bone defects in both primary malignant and metastatic bone tumors.

#### 3.9. In vivo degradation behavior and ion biodistribution

Appropriate degradation behavior of biodegradable implants is essential for mechanical strength and bone healing. The reconstructed micro-CT 3D images without peritumoral tissues of the MAO coated and BP coated Mg implanted for 2 and 4 weeks are used to visually display the degradation trends from the view of space-time. As shown in Fig. 8, all the coated Mg pellets undergo volume reduction during implantation, but at a different level. At 4 W postimplantation, the residual volume of BP-coated Mg pellets is obviously larger than that of the MAO coated Mg pellets. Meanwhile, there are fewer corrosion pits on BP coated Mg pel-

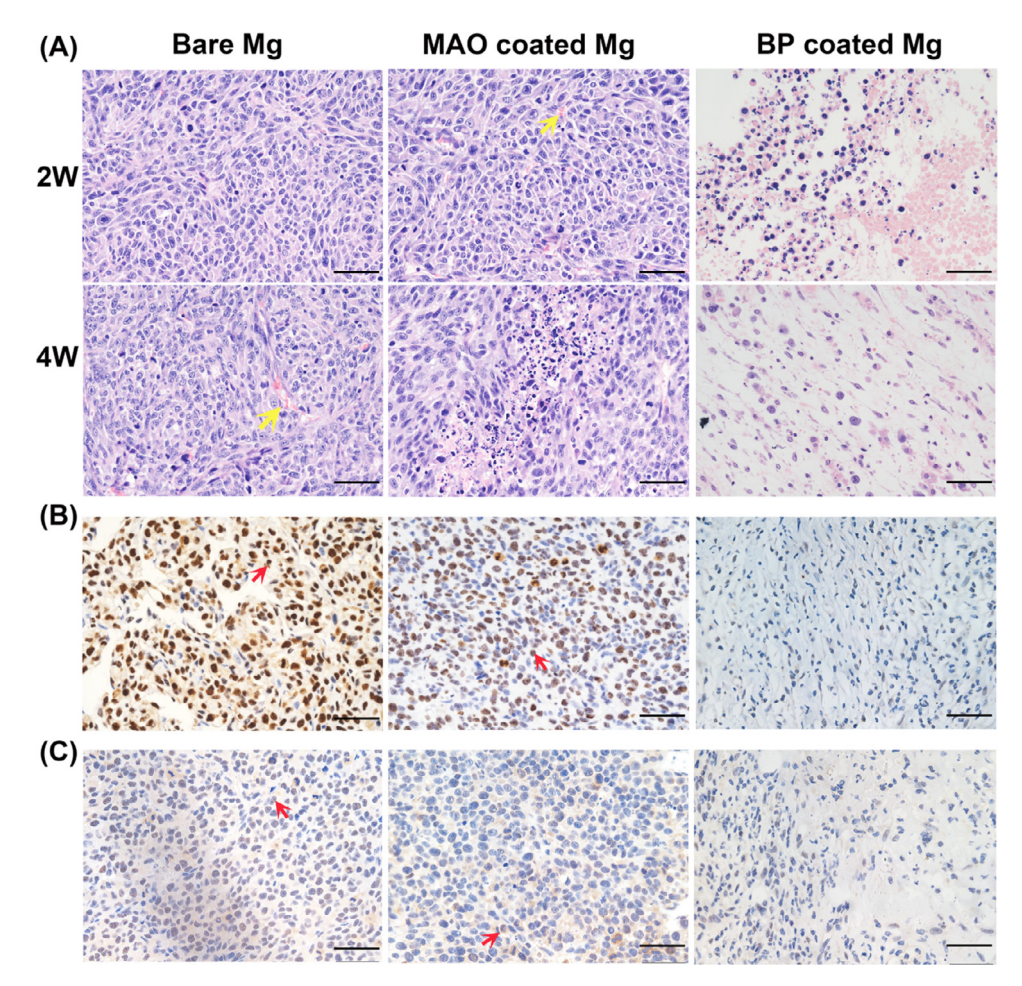


**Fig. 6.** Histological study of tumor tissue surrounding the Mg pellets. (A) H&E staining of tumors collected from different treatments after a 2-week and 4-week implant period. Tumor cells are severely damaged in the BP coated Mg pellet group; however, arrowheads indicate the blood vessel distribution inside the tumor in Mg and MAO coated Mg pellets. (B) Ki-67 IHC staining of tumor tissues. Ki-67 is negatively expressed in BP coated Mg but highly expressed in the other two groups (indicated by brown or dark brown colors). (C) p65 IHC staining of tumor tissues. p65 is negatively expressed in BP coated Mg but highly expressed in the other groups (indicated by brown colors). Scale bar=50  $\mu$ m. (For interpretation of the references to color in this figure legend, the reader is referred to the web version of this article.).

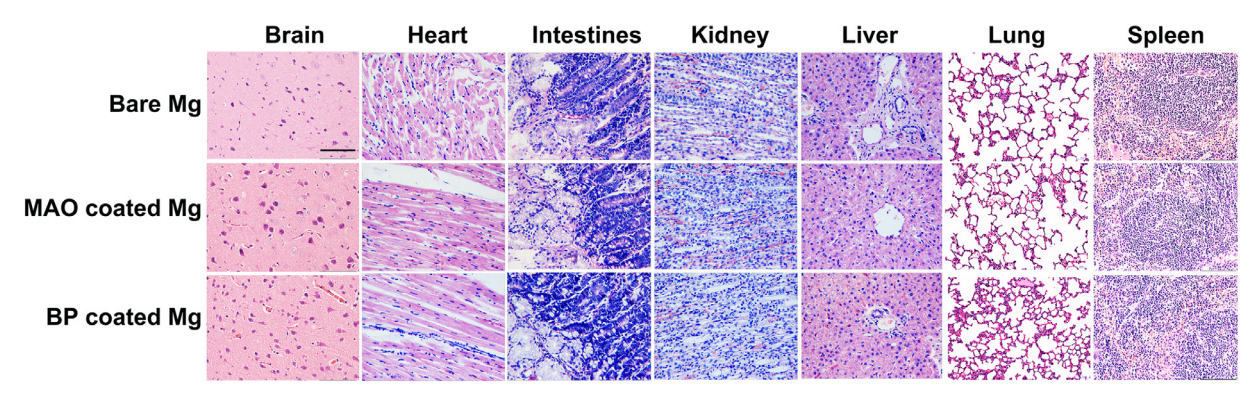


**Fig. 7.** H&E staining of the main organs in the different treatment groups. Scale bar=100  $\mu$ m

lets, indicating the visible corrosion protection of the BP coating in the early stages of *in vivo* implantation. In addition, the average corrosion rates of MAO coated Mg and BP coated Mg pellets measured at 4 W dramatically decrease compared to those measured at 2 W, and the corrosion rate of BP coated Mg is still lower than that of MAO coated Mg at different points in time (p < 0.01).

In addition to the corrosion behaviors of Mg pellets, the biodistribution of metallic elements should also be properly understood because the metabolism of degradation products is closely related

to biocompatibility and tissue repair. Therefore, the concentrations of Mg ions and Sr ions in the main metabolic organs, including the spleen, liver and kidney, as well as blood are carefully quantified over the experimental period by ICP-MS. Fig. 9 shows that the concentration of Mg ions in the kidney gradually increases and reaches a peak at 4 W postimplantation (63.7 mg kg $^{-1}$ ); however, the changes in the Mg ions in the other organs and blood are not noticeable. Unlike this, much of the Sr ions are elevated in the liver, kidney and blood, and the uptake is 1.9 µg kg $^{-1}$ , 4.9 µg kg $^{-1}$ 

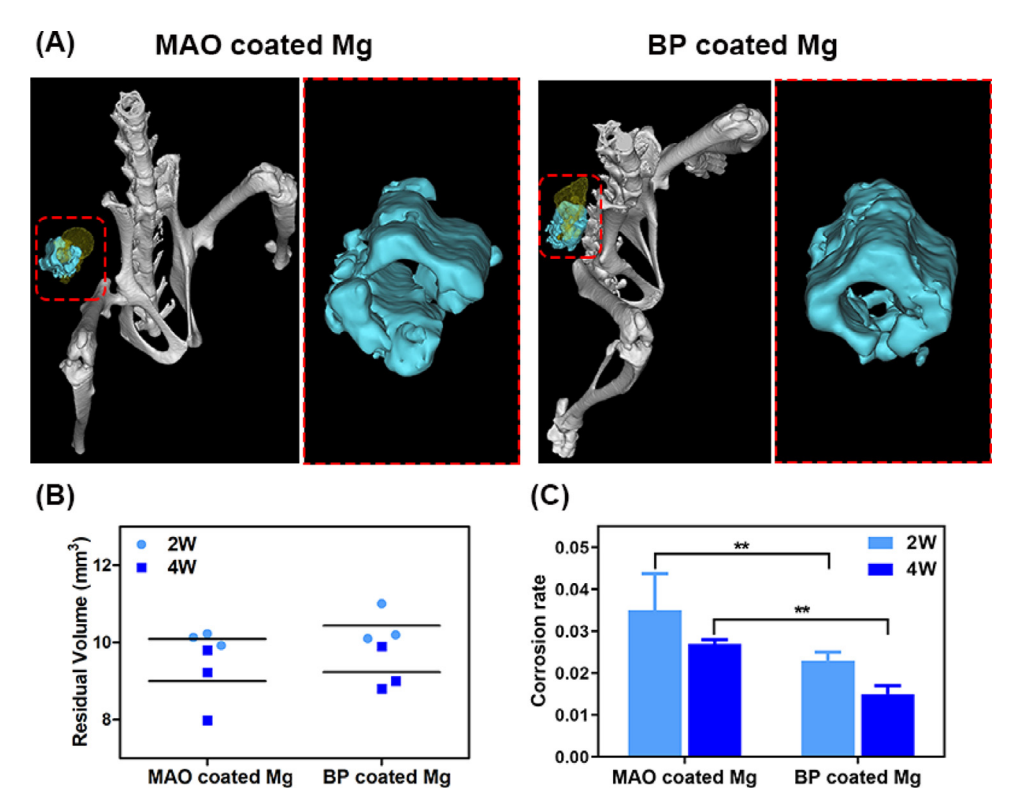


Fig. 8. In vivo CT imaging and corrosion performance of Mg pellets. (A) 3D morphology of MAO coated Mg pellets and BP coated Mg pellets implanted in tumor-bearing mice at 4 W from micro-CT. The corresponding red dotted boxes show high magnification of the circled area. The gas cavity area in the peri-implant tissues is reconstructed to irregular yellow geometry. (B) Residual volumes of the Mg pellets at 2 and 4 weeks after implantation. (C) Corrosion rates of Mg pellets. All data are presented as the mean  $\pm$  standard deviation of three independent experiments. (For interpretation of the references to color in this figure legend, the reader is referred to the web version of this article.)

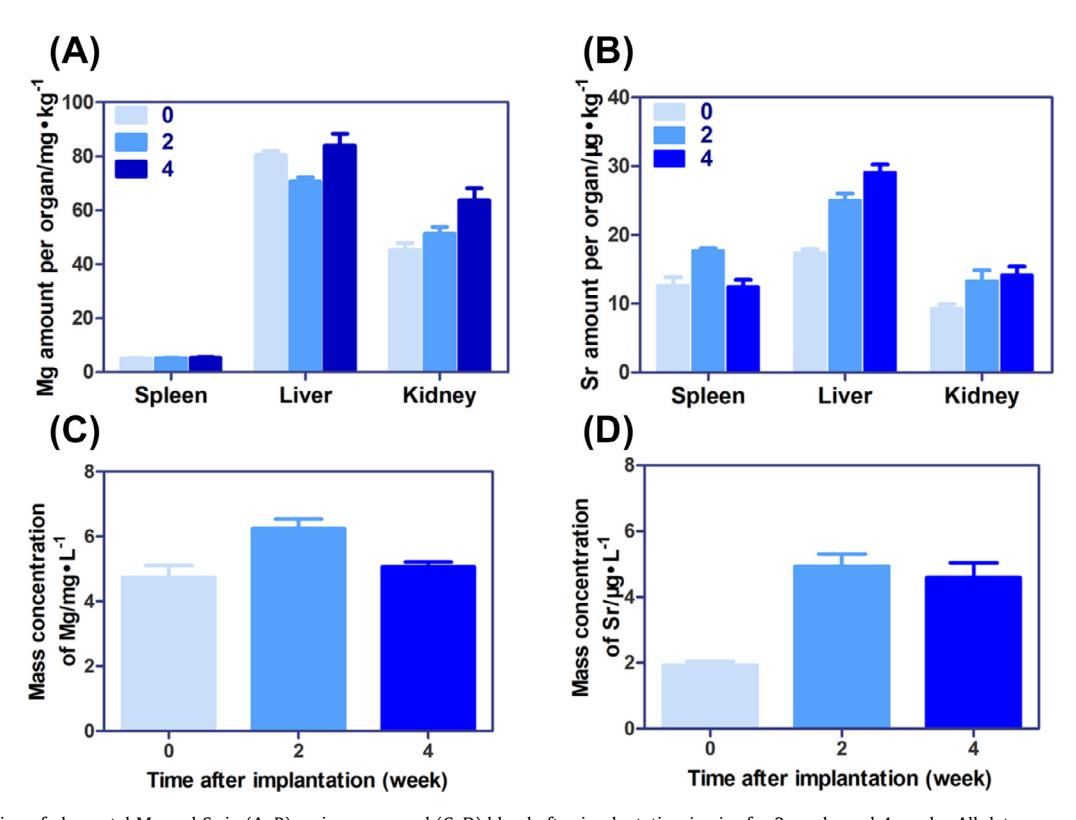


Fig. 9. Biodistribution of elemental Mg and Sr in (A, B) main organs and (C, D) blood after implantation in vivo for 2 weeks and 4 weeks. All data are presented as the mean  $\pm$  standard deviation of the three independent experiments.

and 4.6  $\mu$ g L<sup>-1</sup> at 4 W, respectively. These dynamic results suggest that Mg ions may be slowly excreted through the kidney and that Sr ions may enter the blood and then be metabolized through the liver and kidney.

#### 4. Conclusion

In conclusion, we synthesized a nitrogen-containing bisphosphonate-loaded microarc oxidation coating on biodegradable Mg-Sr alloy pellet and found that the pellets has outstanding results for treating highly malignant OS. The BP coated Mg pellet exhibits good biocompatibility, inductivity of tumor apoptosis and necrosis, as well as inhibitory effects on tumor invasion and cell cycle progression in both in vitro 2D and 3D cell culture environments. After implantation in vivo, the BP coating could, to some extent, protect Mg pellets against corrosion, and BP coated Mg pellets could effectively inhibit tumor recurrence and growth. Furthermore, the BP coated Mg pellets could significantly suppress the mevalonate pathway at the molecular biology level in OS cells compared to other Mg pellets. Above all, the as-synthesized BP coated Mg pellets could be developed as a new candidate for malignant bone tumor therapy combined with surgical operation.

#### **Declaration of Competing Interest**

The authors declare that they have no known competing financial interests or personal relationships that could have appeared to influence the work reported in this paper.

#### Acknowledgment

The authors gratefully acknowledge the financial support from the Natural Science Foundation of Guangdong Province, China (Grant No. 2020A1515011447), the National Key Research Program of China (Grant No. 2017YFB0702604), the National Natural Science Foundation of China (Grant No. 31771038), the Scientific and Technological Projects of Guangzhou, China (Grant No. 202002030283), and research start-up funds of DGUT (No. GC300501-082). All animal experiments were approved and performed in compliance with the local ethics committee and Guangdong Provincial People's Hospital institutional guidelines.

# Supplementary materials

Supplementary material associated with this article can be found, in the online version, at doi:10.1016/j.actbio.2020.11.019.

#### References

- [1] M. Kansara, M.W. Teng, M.J. Smyth, D.M. Thomas, Translational biology of osteosarcoma, Nat. Rev. Cancer 14 (11) (2014) 722–735.
- [2] J. Ritter, S.S. Bielack, Osteosarcoma, Ann. Oncol. 21 (Suppl 7) (2010) vii320-vii325.
- [3] M.A. Anwar, C. El-Baba, M.H. Elnaggar, Y.O. Elkholy, M. Mottawea, D. Johar, T.S. Al Shehabi, F. Kobeissy, C. Moussalem, E. Massaad, I. Omeis, N. Darwiche, A.H. Eid, Novel therapeutic strategies for spinal osteosarcomas, Semin. Cancer Biol. 64 (2020) 83–92.
- [4] R. Veth, R. van Hoesel, M. Pruszczynski, J. Hoogenhout, B. Schreuder, T. Wobbes, Limb salvage in musculoskeletal oncology, Lancet Oncol. 4 (6) (2003) 343–350.
- [5] G. Han, W.Z. Bi, M. Xu, J.P. Jia, Y. Wang, Amputation versus limb-salvage surgery in patients with osteosarcoma: a meta-analysis, World J. Surg. 40 (8) (2016) 2016–2027.
- [6] Y. Li, Y. Sun, H.-C. Shan, X.-H. Niu, Comparative analysis of early follow-up of biologic fixation and cemented stem fixation for femoral tumor prosthesis: biologic fixation and cemented stem fixation for distal femoral tumor prosthesis, Orthop. Surg. 11 (3) (2019) 451–459.
- [7] R.J. Grimer, Surgical options for children with osteosarcoma, Lancet Oncol. 6 (2) (2005) 85–92.
- [8] K.S. Mangat, L.M. Jeys, S.R. Carter, Latest developments in limb-salvage surgery in osteosarcoma, Expert Rev. Anticancer Ther. 11 (2) (2011) 205–215.

[9] K. Zils, S. Bielack, M. Wilhelm, M. Werner, R. Schwarz, R. Windhager, G. Hof-mann-Wackersreuther, T. Andus, L. Kager, T. Kuehne, P. Reichardt, T. von Kalle, Osteosarcoma of the mobile spine, Ann. Oncol. 24 (8) (2013) 2190–2195.

- [10] B.T. Palumbo, E.R. Henderson, J.S. Groundland, D. Cheong, E. Pala, G.D. Letson, P. Ruggieri, Advances in segmental endoprosthetic reconstruction for extremity tumors: a review of contemporary designs and techniques, Cancer Control 18 (3) (2011) 160–170.
- [11] M.J. Coathup, A. Sanghrajka, W.J. Aston, P.D. Gikas, R.C. Pollock, S.R. Cannon, J.A. Skinner, T.W. Briggs, G.W. Blunn, Hydroxyapatite-coated collars reduce radiolucent line progression in cemented distal femoral bone tumor implants, Clin. Orthop. Relat. Res. 473 (4) (2015) 1505–1514.
- [12] W. Zhang, I. Bado, H. Wang, H.C. Lo, X.H. Zhang, Bone metastasis: find your niche and fit in, Trends Cancer 5 (2) (2019) 95–110.
- [13] Y. Zhang, J. Xu, Y.C. Ruan, M.K. Yu, M. O'Laughlin, H. Wise, D. Chen, L. Tian, D. Shi, J. Wang, S. Chen, J.Q. Feng, D.H. Chow, Implant-derived magnesium induces local neuronal production of CGRP to improve bone-fracture healing in rats, Nat. Med. 22 (10) (2016) 1160–1169.
- [14] C. Li, C. Guo, V. Fitzpatrick, A. Ibrahim, M.J. Zwierstra, P. Hanna, A. Lechtig, A. Nazarian, S.J. Lin, D.L. Kaplan, Design of biodegradable, implantable devices towards clinical translation, Nat. Rev. Mater. 5 (1) (2020) 61–81.
- [15] P. Wilflingseder, R. Martin, C. Papp, Magnesium seeds in the treatment of lymph- and haemangiomata, Eur. J. Plast. Surg. 6 (1981) 105–116.
- [16] S. Thierfelder, R. Hagen, J.E. Sold-Darseff, A. Uhlmann, Magnesium seeding in therapy of pediatric hemangioma of the temporal region, lower eyelid and orbit, Klin. Monbl. Augenheilkd. 208 (4) (1996) 243–245.
- [17] F. Witte, The history of biodegradable magnesium implants: a review, Acta Biomater. 6 (5) (2010) 1680–1692.
- [18] M. Li, L. Ren, L. Li, P. He, G. Lan, Y. Zhang, K. Yang, Cytotoxic effect on osteosar-coma MG-63 cells by degradation of magnesium, J. Mater. Sci. Technol. 30 (9) (2014) 888–893.
- [19] M. Li, W. Wang, Y. Zhu, Y. Lu, P. Wan, K. Yang, Y. Zhang, C. Mao, Molecular and cellular mechanisms for zoledronic acid-loaded magnesium-strontium alloys to inhibit giant cell tumors of bone, Acta Biomater. 77 (2018) 365–379.
- [20] B. Ory, M. Baud'huin, F. Verrecchia, B.B. Royer, T. Quillard, J. Amiaud, S. Battaglia, D. Heymann, F. Redini, F. Lamoureux, Blocking HSP90 addiction inhibits tumor cell proliferation, metastasis development, and synergistically acts with zoledronic acid to delay osteosarcoma progression, Clin. Cancer Res. 22 (10) (2016) 2520–2533.
- [21] A.L. Himelstein, J.C. Foster, J.L. Khatcheressian, J.D. Roberts, D.K. Seisler, P.J. Novotny, R. Qin, R.S. Go, S.S. Grubbs, T. O'Connor, M.R. Velasco Jr., D. Weckstein, A. O'Mara, C.L. Loprinzi, C.L. Shapiro, Effect of longer-interval vs standard dosing of zoledronic acid on skeletal events in patients with bone metastases: a randomized clinical trial, JAMA 317 (1) (2017) 48–58.
- [22] T. Ohba, H.A. Cole, J.M. Cates, D.A. Slosky, H. Haro, T. Ando, H.S. Schwartz, J.G. Schoenecker, Bisphosphonates inhibit osteosarcoma-mediated osteolysis via attenuation of tumor expression of MCP-1 and RANKL, J. Bone Miner. Res. 29 (6) (2014) 1431–1445.
- [23] N.M. La-Beck, X. Liu, H. Shmeeda, C. Shudde, A.A. Gabizon, Repurposing amino-bisphosphonates by liposome formulation for a new role in cancer treatment, Semin. Cancer Biol. (19) (2019) 30396–30407 S1044-579X.
- [24] J. Vanderburgh, J.L. Hill, M.K. Gupta, K.A. Kwakwa, S.K. Wang, K. Moyer, S.K. Be-dingfield, A.R. Merkel, R. d'Arcy, S.A. Guelcher, Tuning ligand density to optimize pharmacokinetics of targeted nanoparticles for dual protection against tumor-induced bone destruction, ACS Nano 14 (1) (2020) 311–327.
- [25] J. Han, P. Wan, Y. Ge, X. Fan, L. Tan, J. Li, K. Yang, Tailoring the degradation and biological response of a magnesium-strontium alloy for potential bone substitute application, Mater. Sci. Eng. C Mater. Biol. Appl. 58 (2016) 799–811.
- [26] M. Li, X. Yang, W. Wang, Y. Zhang, P. Wan, K. Yang, Y. Han, Evaluation of the osteo-inductive potential of hollow three-dimensional magnesium-strontium substitutes for the bone grafting application, Mater. Sci. Eng. C Mater. Biol. Appl. 73 (2017) 347–356.
- [27] S. Nath, G.R. Devi, Three-dimensional culture systems in cancer research: focus on tumor spheroid model, Pharmacol. Ther. 163 (2016) 94–108.
- [28] Q. Wu, M. Li, L. Tan, J. Yu, Z. Chen, L. Su, X. Ren, C. Fu, J. Ren, L. Li, F. Cao, P. Liang, Y. Zhang, X. Meng, A tumor treatment strategy based on biodegradable BSA@ZIF-8 for simultaneously ablating tumors and inhibiting infection, Nanoscale Horiz. 3 (6) (2018) 606–615.
- [29] G. Li, L. Zhang, L. Wang, G. Yuan, K. Dai, J. Pei, Y. Hao, Dual modulation of bone formation and resorption with zoledronic acid-loaded biodegradable magnesium alloy implants improves osteoporotic fracture healing: an in vitro and in vivo study, Acta Biomater. 65 (2018) 486–500.
- [30] K. Harnden, K. Blackwell, Routine use of zoledronic acid in early-stage breast cancer, J. Natl. Compr. Cancer Netw. 13 (4) (2015) 480–486.
- [31] R. von Moos, L. Costa, E. Gonzalez-Suarez, E. Terpos, D. Niepel, J.J. Body, Management of bone health in solid tumours: from bisphosphonates to a monoclonal antibody, Cancer Treat. Rev. 76 (2019) 57–67.
- [32] H. Peinado, H.Y. Zhang, I.R. Matei, B. Costa-Silva, A. Hoshino, G. Rodrigues, B. Psaila, R.N. Kaplan, J.F. Bromberg, Y.B. Kang, M.J. Bissell, T.R. Cox, A.J. Giaccia, J.T. Erler, S. Hiratsuka, C.M. Ghajar, D. Lyden, Pre-metastatic niches: organ-specific homes for metastases, Nat. Rev. Cancer 17 (5) (2017) 302–317.
- [33] A.W. Lambert, D.R. Pattabiraman, R.A. Weinberg, Emerging biological principles of metastasis, Cell 168 (4) (2017) 670–691.
- [34] M.S. D'Arcy, Cell death: a review of the major forms of apoptosis, necrosis and autophagy, Cell Biol. Int. 43 (6) (2019) 582–592.

- [35] D. Kogel, B. Linder, A. Brunschweiger, S. Chines, C. Behl, At the crossroads of apoptosis and autophagy: multiple roles of the co-chaperone BAG3 in stress and therapy resistance of cancer, Cells 9 (3) (2020) 574.
- [36] Q. Feng, X. Yang, Y. Hao, N. Wang, X. Feng, L. Hou, Z. Zhang, Cancer cell membrane-biomimetic nanoplatform for enhanced sonodynamic therapy on breast cancer via autophagy regulation strategy, ACS Appl. Mater. Interfaces 11 (36) (2019) 32729–32738.
- [37] G.I. Evan, K.H. Vousden, Proliferation, cell cycle and apoptosis in cancer, Nature 411 (6835) (2001) 342–348.
- [38] M.B. Kastan, J. Bartek, Cell-cycle checkpoints and cancer, Nature 432 (7015) (2004) 316–323.
- [39] S. Goel, M.J. DeCristo, A.C. Watt, H. BrinJones, J. Sceneay, B.B. Li, N. Khan, J.M. Ubellacker, S. Xie, O. Metzger-Filho, J. Hoog, M.J. Ellis, C.X. Ma, S. Ramm, I.E. Krop, E.P. Winer, T.M. Roberts, H.J. Kim, S.S. McAllister, J.J. Zhao, CDK4/6 inhibition triggers anti-tumour immunity, Nature 548 (7668) (2017) 471–475.
- [40] R. Roskoski, Cyclin-dependent protein serine/threonine kinase inhibitors as anticancer drugs, Pharmacol. Res. 139 (2019) 471–488.
- [41] T. Otto, P. Sicinski, Cell cycle proteins as promising targets in cancer therapy, Nat. Rev. Cancer 17 (2) (2017) 93–115.
- [42] H. Qiao, T. Tang, Engineering 3D approaches to model the dynamic microenvironments of cancer bone metastasis, Bone Res. 6 (2018) 3.
- [43] P.J. Mullen, R. Yu, J. Longo, M.C. Archer, L.Z. Penn, The interplay between cell signalling and the mevalonate pathway in cancer, Nat. Rev. Cancer 16 (11) (2016) 718–731.
- [44] S.H. Moon, C.H. Huang, S.L. Houlihan, K. Regunath, W.A. Freed-Pastor, J.P.t. Morris, D.F. Tschaharganeh, E.R. Kastenhuber, A.M. Barsotti, R. Culp-Hill, W. Xue, Y.J. Ho, T. Baslan, X. Li, A. Mayle, E. de Stanchina, L. Zender, D.R. Tong, A. D'Alessandro, S.W. Lowe, C. Prives, Represses the mevalonate pathway to mediate tumor suppression, Cell 176 (3) (2019) 564–580 e19.
- [45] Y. Xia, Y. Xie, Z. Yu, H. Xiao, G. Jiang, X. Zhou, Y. Yang, X. Li, M. Zhao, L. Li, M. Zheng, S. Han, Z. Zong, X. Meng, H. Deng, H. Ye, Y. Fa, H. Wu, E. Oldfield, X. Hu, W. Liu, Y. Shi, Y. Zhang, The mevalonate pathway is a druggable target for vaccine adjuvant discovery, Cell 175 (4) (2018) 1059–1073.
- [46] Q. Tang, S. Jiang, W. Jia, D. Shen, Y. Qiu, Y. Zhao, B. Xue, C. Li, Zoledronic acid, an FPPS inhibitor, ameliorates liver steatosis through inhibiting hepatic de novo lipogenesis, Eur. J. Pharmacol. 814 (2017) 169–177.
- [47] L. Pietrovito, G. Comito, M. Parri, E. Giannoni, P. Chiarugi, M.L. Taddei, Zole-dronic acid inhibits the RhoA-mediated amoeboid motility of prostate cancer cells, Curr. Cancer Drug Targets 19 (10) (2019) 807–816.

- [48] A. Gobel, S. Thiele, A.J. Browne, M. Rauner, V.M. Zinna, L.C. Hofbauer, T.D. Rachner, Combined inhibition of the mevalonate pathway with statins and zoledronic acid potentiates their anti-tumor effects in human breast cancer cells, Cancer Lett. 375 (1) (2016) 162–171.
- [49] X. Dai, H. Xia, S. Zhou, Q. Tang, F. Bi, Zoledronic acid enhances the efficacy of the MEK inhibitor trametinib in KRAS mutant cancers, Cancer Lett. 442 (2019) 202–212.
- [50] I. Kaymak, C.R. Maier, W. Schmitz, A.D. Campbell, B. Dankworth, C.P. Ade, S. Walz, M. Paauwe, C. Kalogirou, H. Marouf, M.T. Rosenfeldt, D.M. Gay, G.H. McGregor, O.J. Sansom, A. Schulze, Mevalonate pathway provides ubiquinone to maintain pyrimidine synthesis and survival in p53-deficient cancer cells exposed to metabolic stress, Cancer Res. 80 (2) (2020) 189–203.
- [51] H. Ma, C. Feng, J. Chang, C. Wu, 3D-printed bioceramic scaffolds: from bone tissue engineering to tumor therapy, Acta Biomater. 79 (2018) 37–59.
- [52] M. Dowless, C.D. Lowery, T. Shackleford, M. Renschler, J. Stephens, R. Flack, W. Blosser, S. Gupta, J. Stewart, Y. Webster, J. Dempsey, A.B. VanWye, P. Ebert, P. Iversen, J.B. Olsen, X. Gong, S. Buchanan, P. Houghton, L. Stancato, Abemaciclib is active in preclinical models of Ewing sarcoma via multipronged regulation of cell cycle, DNA methylation, and interferon pathway signaling, Clin. Cancer Res. 24 (23) (2018) 6028–6039.
- [53] K.L. Henry, D. Kellner, B. Bajrami, J.E. Anderson, M. Beyna, G. Bhisetti, T. Cameron, A.G. Capacci, A. Bertolotti-Ciarlet, J. Feng, B. Gao, B. Hopkins, T. Jenkins, K. Li, T. May-Dracka, P. Murugan, R. Wei, W. Zeng, N. Allaire, A. Buckler, C. Loh, P. Juhasz, B. Lucas, K.A. Ennis, E. Vollman, E. Cahir-McFarland, E.C. Hett, M.L. Ols, CDK12-mediated transcriptional regulation of noncanonical NF-κB components is essential for signaling, Sci. Signal. 11 (541) (2018) eaam8216.
- [54] A.A. Grosset, V. Ouellet, C. Caron, G. Fragoso, V. Barrès, N. Delvoye, M. Latour, A. Aprikian, A. Bergeron, S. Chevalier, L. Fazli, N. Fleshner, M. Gleave, P. Karakiewicz, L. Lacombe, J.B. Lattouf, T. van der Kwast, D. Trudel, A.M. Mes-Masson, F. Saad, Validation of the prognostic value of NF-κB p65 in prostate cancer: a retrospective study using a large multi-institutional cohort of the Canadian prostate cancer biomarker network, PLoS Med. 16 (7) (2019) e1002847.
- [55] S. Otto, C. Pautke, C. Opelz, I. Westphal, I. Drosse, J. Schwager, F. Bauss, M. Ehrenfeld, M. Schieker, Osteonecrosis of the jaw: effect of bisphosphonate type, local concentration, and acidic milieu on the pathomechanism, J. Oral. Maxillofac. Surg. 68 (11) (2010) 2837–2845.